

Active Sampling for MRI-based Sequential Decision Making

Yuning Du^{a,*}, Jingshuai Liu^a, Rohan Dharmakumar^b, Sotirios A. Tsaftaris^a

^a*School of Engineering, The University of Edinburgh, 5 Little France Rd, Edinburgh, EH16 4UX, Scotland, United Kingdom*

^b*School of Medicine, Indiana University, 340 West 10th Street, Indianapolis, IN 46202-3082, Indiana, United States*

Abstract

Despite the superior diagnostic capability of Magnetic Resonance Imaging (MRI), its use as a Point-of-Care (PoC) device remains limited by high cost and complexity. To enable such a future, one key approach will be to improve sampling strategies. Previous work has shown that it is possible to make diagnostic decisions directly from k -space with fewer samples. Such work shows that single diagnostic decisions can be made, but if we aspire to see MRI as a true PoC, multiple and sequential decisions are necessary while minimizing the number of samples acquired. We present a novel multi-objective reinforcement learning framework enabling comprehensive, sequential, diagnostic evaluation from undersampled k -space data. Our approach during inference actively adapts to sequential decisions to optimally sample. To achieve this, we introduce a training methodology that identifies the samples that contribute the best to each diagnostic objective using a step-wise weighting reward function. We evaluate our approach in two sequential knee pathology assessment tasks: ACL sprain detection and cartilage thickness loss assessment. Our framework achieves diagnostic performance competitive with various policy-based benchmarks across disease detection, severity quantification, and overall sequential diagnosis, while substantially reducing the number of required k -space samples, thereby advancing MRI toward a more comprehensive and affordable point-of-care device.

Keywords: Computer aided diagnosis, Magnetic resonance imaging, Point

*Corresponding author.

Email address: yuning.du@ed.ac.uk (Yuning Du)

1. Introduction

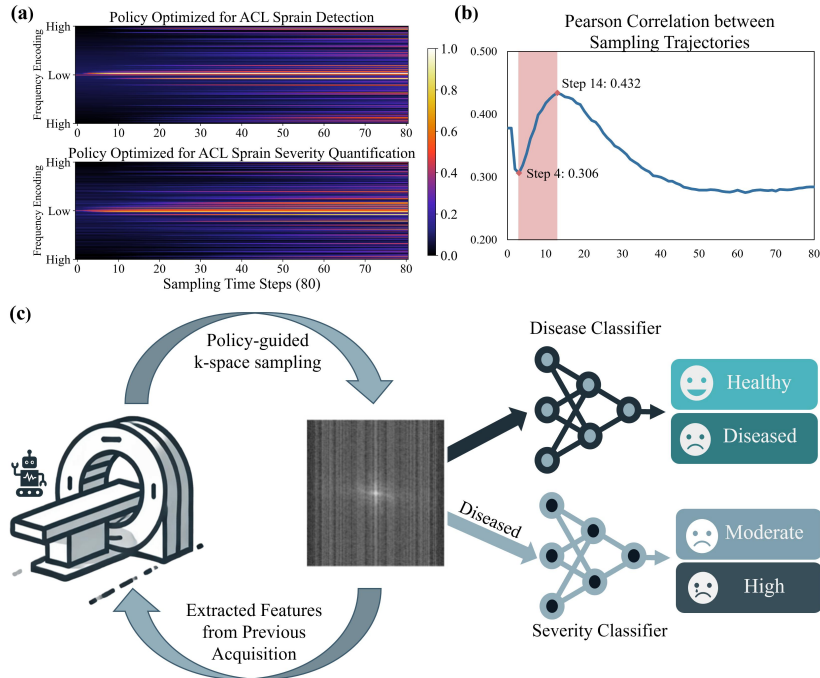


Figure 1: Illustration of our proposed sequential diagnostic framework for active MR acquisition and its motivating evidence. In preliminary experiments, we found similarities between the sampling trajectories of disease detection and severity quantification. We have trained policies (Du et al., 2024) optimized independently for each task and obtained sampling trajectories shown in (a), and then measure their similarity in (b). We observe an increasing Pearson correlation between sampling steps 4 and 14, indicating that in this range k -space samples contribute simultaneously to both tasks. These observations motivate our approach (c) to learn a sampling policy that jointly optimizes two tasks, taking into account their sequential nature. During inference, our approach identifies which samples to take using k -space features, considering that one task (severity) will be following the confirmation of the disease.

Despite the proliferation of MRI, its utility as a Point-Of-Care (PoC) diagnostic tool remains limited due to prolonged acquisition times, complex instrumentation, and high cost (Geethanath and Vaughan Jr, 2019). A promising solution has emerged through the development of low-field MRI

systems (Anzai and Moy, 2022). These systems can be deployed at accident sites, in ambulatory settings, or in other areas where immediate decisions are necessary to provide the best treatment options. Thus, such PoC settings are not to replace the utility of MRI as a clinical generic diagnostic tool, but as a bespoke affordable and portable device. However, a reduced magnetic field strength (Hori et al., 2021) does degrade imaging quality. Therefore, improvements in how and where we sample are considered key for unlocking the future of MRI as PoC.

Recent advances in machine learning methods have allowed a reduction in k -space samples and retaining diagnostic utility (Lin et al., 2021). A line of work has focused on optimizing sampling trajectories for image reconstruction (Bahadir et al., 2020; Zhang et al., 2019). More recently, exciting approaches have emerged that aim to drastically reduce sampling by removing redundant information. These methods bypass image reconstruction entirely and make direct inferences from undersampled k -space (Singhal et al., 2023; Yen et al., 2024).

Decisions even in a PoC setting will be complex and reflect a multilayered decision making process. Hence, high-level decisions (e.g., disease presence) should be made first, followed by additional decisions (e.g., disease severity) to determine subsequent actions (e.g., treatment options). A fundamental research question emerges: *Are there correlations in k -space patterns between such sequential decisions and can these be exploited for further sampling reductions?* If such correlations exist, sampling strategies should be optimized to exploit them. Otherwise, independently optimizing sampling strategies for each diagnostic task leads to sampling inefficiency. Our preliminary experiments (Figure 1) reveal compelling correlation patterns between sampling trajectories.

Leveraging this observation, we develop an AI agent to satisfy both objectives within the same policy, maintaining computational efficiency while structuring binary diagnostics as a structured sequential decision process for comprehensive clinical assessment. To the best of our knowledge, such active sampling strategies for sequential diagnostic tasks have not been previously explored. We reformulate the diagnostic process as a multi-objective reinforcement learning (MORL) sampling optimization problem, sequentially inferring the presence of the disease and its severity in one scanning session.

As illustrated in Figure 1, the core components of our framework include: an RL-based policy network for k -space sampling guidance, and dual diagnostic streams for disease detection and severity quantification. The

policy network guides data acquisition by leveraging features extracted from accumulated k -space measurements, continuously optimizing the sampling trajectory. The diagnostic streams process the undersampled k -space hierarchically: the disease classifier performs binary classification to identify diseased subjects, which is followed by severity quantification for positive cases.

Overall, our **contributions** are summarized as follows:

- Our research pioneers sequential, dynamic diagnosis from k -space data with active sampling, providing sequential decisions in a single scanning session.
- A policy gradient based network with greedy action selection enables efficient k -space exploration and patient-level sampling adaptation.
- A step-wise weighting reward function is proposed to balance disease detection and severity quantification during policy training, maximizing diagnostic information gain.
- Extensive experiments on ACL sprain detection and cartilage thickness loss assessment demonstrate that our method outperforms baselines and benchmarks in diagnostic accuracy, and significantly reduces k -space data acquisition time, advancing PoC MRI applications.

2. Related Works

We first review ML-based k -space sampling optimization techniques that accelerate acquisition. We then examine direct diagnostic inference approaches from k -space, highlighting the research gap in sequential decision making. Finally, we discuss RL-based multi-objective optimization in medical imaging, demonstrating how our sequential sampling framework builds upon these foundations to enable comprehensive diagnosis directly from undersampled k -space.

2.1. ML-based k -space Sampling Optimization

Accelerating MRI acquisition remains a significant research focus through improved k -space undersampling strategies. While the Cartesian grid trajectory predominates in clinical practice due to its robustness (Zeng et al., 2021), conventional undersampling approaches—including equispaced, random, and variable density sampling—prioritize frequency domain characteristics rather than task-specific requirements, potentially compromising clinical accuracy in accelerated acquisitions (Yiasemis et al., 2024).

Recent works have advanced learning-based sampling methods that optimize diagnostic performance at the population level. These approaches formulate sampling mask optimization either as a probability density function for Cartesian grid selection (Bahadir et al., 2020; Wang et al., 2022b; Martinini et al., 2022; Aggarwal and Jacob, 2020) or as learnable non-Cartesian coordinates (Zhang et al., 2020; Chaithya et al., 2022) in non-uniform Fast Fourier Transform (NUFFT) (Wang et al., 2022a; Wang and Fessler, 2023; Alkan et al., 2020), enabling end-to-end optimization of sampling trajectories and reconstruction performance. Advancements have also been made in co-design frameworks that jointly optimize sampling, reconstruction, and prediction strategies for enhanced performance on downstream tasks (Wu et al., 2024). While subsequent innovations incorporate generative models (Ravula et al., 2023) and model pruning (Xuan et al., 2020), these methods produce fixed sampling patterns that do not adapt to patient-specific characteristics.

Instead, active sampling strategies adapt to individual patients through sequential k -space measurements. Reinforcement learning (RL) has emerged as a powerful framework for this sampling optimization, framing k -space sampling as a Markov Decision Process where policies learn to select measurements based on accumulated information. Notable approaches include policy gradient methods with greedy actions (Bakker et al., 2020) and Q-learning (Pineda et al., 2020) for reconstruction optimization. While initial work focused on reconstruction quality, recent studies demonstrate the potential for direct diagnostic inference from undersampled data (Schlemper et al., 2018; Li et al., 2024), indicating a paradigm shift from traditional reconstruction-based analysis to efficient, direct k -space diagnostic assessment.

2.2. Direct Diagnostic Inference from k -space

A new line of work has shown the potential of ‘image-less’ diagnostic processes through direct inference from k -space data. This approach reduces the need for reconstruction, saving samples by avoiding redundant and uninformative pixels (voxels). Studies show successful disease classification (Du et al., 2024; Singhal et al., 2023; Yen et al., 2024; Li et al., 2024), segmentation (Schlemper et al., 2018; Li et al., 2024), and regression (Li et al., 2024) using undersampled k -space measurements, without reconstructing images. Direct inference with population-level undersampling optimization achieves comparable performance to fully-sampled image analysis, while integration with RL-based active sampling enables patient-level mask optimization and

improved classification performance (Du et al., 2024; Yen et al., 2024). However, existing approaches primarily optimize sampling for a single objective during a scanning session, leaving multi-objective sampling optimization unexplored. As such any additional redundancy between the sampling patterns for different tasks (and hence different objectives) is unutilized.

2.3. RL-based Multi-objective Optimization in Medical Imaging

Multi-objective optimization in clinical evaluation systems presents a fundamental challenge in medical imaging. While multi-task learning frameworks have been explored extensively (Zhao et al., 2023; Huang et al., 2021), the joint optimization of sampling strategies for multiple diagnostic targets remains underexplored. Recent advances in MORL show promising methodological innovations across medical applications (Yu et al., 2021). In chest X-ray generation (Han et al., 2024), policy-based RL simultaneously optimizes posture alignment, diagnostic conditions, and multimodal consistency through cumulative reward maximization. Similarly, anatomical landmark detection (Vlontzos et al., 2019) leverages multi-agent frameworks with specialized joint detection while preserving anatomical constraints. Further innovations include consequence-oriented reward functions for simultaneous vertebral detection and segmentation (Zhang et al., 2021), incorporating exponentially weighted attention metrics for balanced task performance.

While various frameworks demonstrate efficacy through weighted rewards (Zhang et al., 2021; Khatami and Gopalappa, 2021) and collaborative strategies (Vlontzos et al., 2019; Liao et al., 2020), their application to k -space sampling optimization remains unexplored, presenting opportunities for frameworks that simultaneously optimize multiple diagnostic goals.

3. Methodology

3.1. Preliminaries

Instead of directly imaging human anatomy, MRI captures the electromagnetic activity in the body after exposure to magnetic fields and radio-frequency pulses, measured in k -space (i.e., the frequency domain). For a single coil measurement, the k -space data can be represented as a 2-dimensional complex-valued matrix $\mathbf{x} \in \mathbb{C}^{r \times c}$, where r is the number of rows and c is the number of columns, respectively. The spatial representation $\mathbf{SR} \in \mathbb{C}^{r \times c}$ is obtained by applying the inverse Fourier Transform to \mathbf{x} , denoted as $\mathbf{SR} = \mathcal{F}^{-1}(\mathbf{x})$, preserving both the magnitude and phase information. The

spatial image $\mathbf{I} \in \mathbb{R}^{r \times c}$ retains only the magnitude of \mathbf{SR} , computed as $\mathbf{I} = |\mathbf{SR}|$, to provide an interpretable representation in image space. The undersampled k -space, represented as \mathbf{x}_u , is modeled by $\mathbf{x}_u = U_L \circ \mathbf{x}$ where U_L can be viewed as a binary mask $U \in \{0, 1\}^{r \times c}$ with L measurements sampled in k -space. The undersampled representation is denoted as $\mathbf{SR}_u = \mathcal{F}^{-1}(\mathbf{x}_u)$.

We exclusively consider a Cartesian mask for MRI undersampling. While non-Cartesian trajectories (e.g., radial, spiral) can offer more efficient k -space coverage, the Cartesian grid was chosen for its widespread clinical prevalence and methodological simplicity (Ayde et al., 2025). This choice avoids the complex gridding steps required by other types of trajectories which could introduce confounding artifacts, and thereby ensures a clear and direct evaluation of our adaptive sampling policy.

For clinical diagnosis, radiologists and other clinical experts interpret medical imaging data to first identify the presence of disease (g_d) and then its severity (g_s), providing a comprehensive diagnosis. These labels are derived by analyzing the collected k -space data after appropriate processing.

3.2. Framework Workflow

As shown in Figure 2, our framework aims to reduce acquisition time by selectively and progressively sampling the k -space, considering sequential diagnostic tasks.

The process begins with a small subset of randomly sampled k -space with L measurements, denoted as $\mathbf{x}_{u_0} = U_L \circ \mathbf{x}$, which is passed to task-specific classifiers. The pre-trained disease and severity classification networks f_d and f_s , generate the initial disease and severity prediction y_{d_0} and y_{s_0} . The high-level feature maps m_0 , from the last two layers of both classifiers, are extracted and stacked. The feature maps are then fed into the *Active Sampler* S , where the policy network, parameterized by ϕ , generates a sampling policy $\pi_\phi(m_0)$ to guide the selective sampling of diagnostically significant lines in the k -space. These sampled lines are subsequently added to U_L . The updated k -space subset at step $t \in [0, T]$ is denoted as $\mathbf{x}_{u_t} = U_t \circ \mathbf{x}$ and fed back into the classification network. The iterative process continues until the sampling budget T is exhausted or some user-defined reliability criterion (e.g., confidence score) is satisfied. The closed-loop design of the inference stage is presented in Algorithm 1.

During training, we separately calculate the disease reward r_d and severity reward r_s using classifier predictions and the ground truth labels. An obvious and naive approach would be to directly use the rewards to supervise the

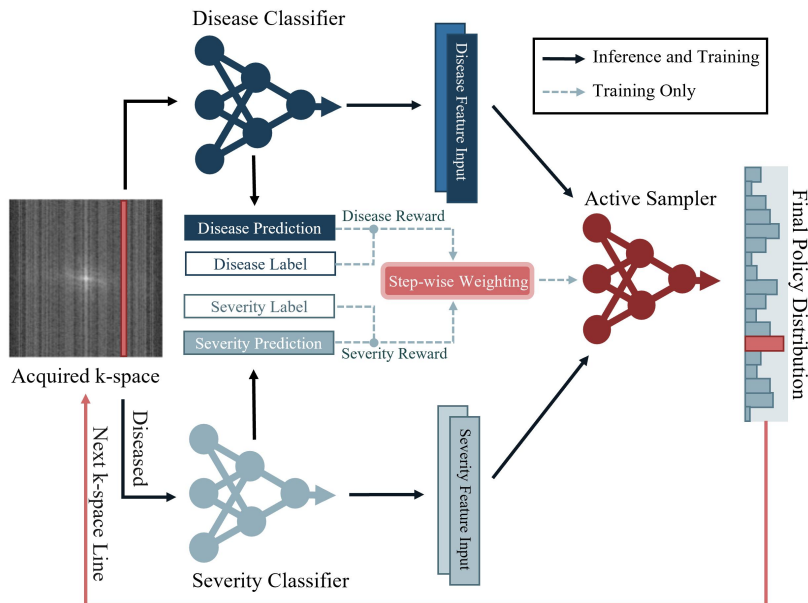


Figure 2: Illustration of the proposed sequential diagnostic active sampling. Initially, a randomly sampled k -space subset is fed into two pre-trained disease and severity classifiers. The active sampler takes as input the features extracted by the classifiers and decides the next k -space sampling location. After exhausting the sampling budget or meeting a user-defined criterion, the disease classifier confirms the presence of disease and subsequently the severity classifier is queried to estimate the severity level. During training, the active sampler is optimized with a novel step-wise weighting mechanism that combines the disease and severity rewards and enables a smooth transition.

active sampler; however, this will not learn the sequential aspect of the two objectives. Instead, we propose here to use a step-wise weighting procedure to shift the emphasis of sampling strategy from one objective to the other as sampling steps progress. In addition, to further enforce the sequential nature (i.e., disease prediction should precede severity), if the disease prediction is ‘No findings’ for a subject, the severity reward will not be applied for supervision.

3.3. Undersampled k -Space Classification Networks

To perform prediction with undersampled k -space data, we pre-train a disease classifier f_d with the undersampled representation derived from undersampled k -space data and ground truth label g_d . For the severity classifier f_s , we fine-tune the disease classifier with only diseased data and the associ-

ated severity labels g_s . For severity quantification, fine-tuning prevents potential overfitting caused by data scarcity and reuses the knowledge learned by the disease classifier. These pre-trained classifiers act as the reward model in the training process of the active sampler. They also function as a feature extractor, providing complex and informative feature maps m_t per sampling step as part of the internal state.

Algorithm 1 Closed-loop Active Sampling Inference

Require: Pretrained disease classifier f_d , pretrained severity classifier f_s , policy π_ϕ , initial Cartesian mask U_L with L lines, sampling budget T , underlying k -space x

- 1: $x_u^0 \leftarrow U_0 \circ x$ with $U_0 \leftarrow U_L$ ▷ Acquire initial subset
- 2: $(y_d^0, y_s^0) \leftarrow (f_d(x_u^0), f_s(x_u^0))$ ▷ Initial predictions
- 3: $m^0 \leftarrow \text{EXTRACTFEATURES}(f_d, f_s)$ ▷ High-level feature maps from both streams
- 4: **for** $t = 0, 1, \dots, T - 1$ **do**
- 5: $p \leftarrow \pi_\phi(m^t)$ ▷ Policy over High-level feature maps
- 6: $a_t \leftarrow \arg \max_{\ell \in \mathcal{L} \setminus U_t} p[\ell]$ ▷ Select next line (inference: 1 line/step)
- 7: $U_{t+1} \leftarrow U_t \cup \{a_t\}$ ▷ Update mask
- 8: $x_u^{t+1} \leftarrow U_{t+1} \circ x$ ▷ Acquire measurement at line a_t
- 9: $y_d^{t+1} \leftarrow f_d(x_u^{t+1}); y_s^{t+1} \leftarrow f_s(x_u^{t+1})$ ▷ Update predictions
- 10: $m^{t+1} \leftarrow \text{EXTRACTFEATURES}(f_d, f_s)$ ▷ Update internal state
- 11: **end for**
- 12: $\hat{y}_d \leftarrow y_d^T$
- 13: **if** $\text{ISPOSITIVE}(\hat{y}_d)$ **then**
- 14: $\hat{y}_s \leftarrow y_s^T$ ▷ Severity only reported for disease-positive cases
- 15: **else**
- 16: $\hat{y}_s \leftarrow \text{NOTAPPLICABLE}$
- 17: **end if**
- 18: **return** \hat{y}_d, \hat{y}_s

3.4. Multi-objective k -Space Active Sampler

3.4.1. Problem Formulation

Building on prior works in RL-based k -space active sampling strategies (Du et al., 2024; Bakker et al., 2020; Pineda et al., 2020), the sequential selection of k -space is formalized as a Partially Observable Markov Decision Process (POMDP) (Sondik, 1971).

The latent state z_t at acquisition step t is defined as $z_t = (\mathbf{x}, g_d, g_s, h_t)$, where \mathbf{x} represents the underlying MRI k -space, g_d and g_s denote the disease condition and severity levels, and h_t encapsulates the history of actions and observations up to time t as $h_t = (a_0, o_0, \dots, a_{t-1}, o_{t-1})$. Each action a_t corresponds to the selection of a specific k -space line for measurement, while o_t represents the corresponding measurement obtained from that location. The inclusion of \mathbf{x} in the latent state represents the ground truth data

from which k -space measurements are derived, fundamentally linking the observation model to the true anatomical structure. The agent maintains an internal state composed of high-level features m_t that combine disease and severity features from the corresponding classifiers, and predictions y_t including disease prediction y_{d_t} and severity prediction y_{s_t} , which summarize the history h_t . The agent outputs a policy $\pi(a_t|m_t)$ over possible k -space line selections with only high-level feature representation as input. The reward function $r(z_t, a_t)$ reflects improvements in both disease classification and severity quantification accuracy, weighting their respective contributions through a step-wise mechanism, as discussed below.

3.4.2. Policy Gradient-based Sampler with Greedy Action

In our framework, the POMDP problem is solved via Policy Gradient with greedy action. Specifically, we maximize the expected return $J(\phi)$ of a policy π_ϕ parameterized by ϕ . At each step, the overall classification improvement is calculated as $r(y_{t+1}, y_t) = \eta(y_t, g) - \eta(y_{t+1}, g)$, where r represents the reward computed with criterion η (cross entropy) between predictions y and ground truth labels $g = (g_d, g_s)$.

During training, we accelerate the learning process by sampling q lines with the highest policy probabilities in parallel. The greedy selection method facilitates efficient action space exploration. Technically, we average their accumulated action rewards as feedback for model optimization (Kool et al., 2019) and randomly select one of the q samples as the executed action of the policy. As no greedy action is applied during inference, the trained policy samples one line at each step. We sample q lines at each step to calculate the following estimator:

$$\nabla_\phi J(\phi) \approx \frac{1}{q-1} \mathbb{E}_{\mathbf{x}} \left[\sum_{i=1}^q \sum_{t=L}^{T-1} [\nabla_\phi \log \pi_\phi(m_t)] (r_{i,t} - \frac{1}{q} \sum_{j=1}^q r_{j,t}) \right], \quad (1)$$

where $r_{i,t}$ is the reward of sample i at step t . This equation estimates the gradient $\nabla_\phi J(\phi)$ to update the policy π_ϕ .

3.4.3. Step-wise Reward Weighting with Lexicographic Ordering

As mentioned in Sec. 2.3, a crucial challenge in multi-objective k -space sampling is to jointly optimize multiple objectives without compromising performance. One naive solution is to respectively compute the rewards for the two tasks (here disease detection and severity quantification) and use the

Table 1: Objectives, Diagnostic Support, and Inference Data of Implemented Methods. The objective of Policy Recon is image reconstruction

Method	Diagnostic Objectives			Diagnostic Strengths		Data Used for Inference	
	Disease Detection	Severity Quantification	Overall Diagnosis	Sampling Optimization	Sequential Diagnosis	Undersampled k -space	Full k -space
<i>Fully Sampled</i>	◦	◦	◦				✓
<i>Undersampled</i>	◦	◦	◦			✓	
<i>Policy Recon (Bakker et al., 2020)</i>	-	-	-	✓		✓	
<i>Policy Classifier (Du et al., 2024)</i>	◦	◦	-	✓		✓	
<i>Simulated Policy</i>			◦	✓		✓	
<i>Varying Parameter Policy</i>	•	•	-	✓		✓	
<i>Random Policy</i>	-	-	-			✓	
<i>Weighted Policy (Ours)</i>	•	•	•	✓	✓	✓	✓

◦ : Objective optimized independently (one objective per strategy) • : Multiple objectives optimized simultaneously within a single strategy

total reward as feedback for policy update. However, this ignores the natural order of these two tasks: one first detects disease presence and only if disease is present, the degree of severity is quantified, which aligns with the standard interpretation workflow of radiologists (Royal College of Radiologists, 2018). Following such diagnostic order, we expect the sampling framework to primarily promote disease detection performance in the early stage and focus on severity quantification in the later stage. Consequently, to accomplish these tasks with MORL, we formulate the process as a lexicographic ordering problem (Skalse et al., 2022), where the order of the two objectives is fixed and the weight is dynamically adjusted by *cosine interpolation* (Maeland, 1988) during the sampling process to ensure a smooth transition. Thus, we define a step-wise weighting reward with cosine interpolation for each sample as follows:

$$r_t = w_{disease}(t) * r_d(t) + w_{severity}(t) * r_s(t) \quad (2a)$$

$$w_{severity}(t) = \frac{1}{2} \left(1 - \cos\left(\pi \cdot \frac{t+1}{T} + \pi\beta\right) \right) \quad (2b)$$

$$w_{disease}(t) = 1 - w_{severity}(t), \quad (2c)$$

where r_d and r_s denote disease detection and severity quantification rewards, t is the current step, T is the total acquisition steps, and β denotes a weight parameter which adjusts the equal weighting point. Here we set β to be 0.2 to enable an early transition. The transition of the two objectives is also illustrated in Figure 3. It is shown that by step-wise weighting, the reward function emphasizes the feedback of the disease detection task in the early stage and smoothly transitions to severity quantification. Different β values enable different transition patterns, which can be adjusted based on the complexity and importance of the two optimized objectives.

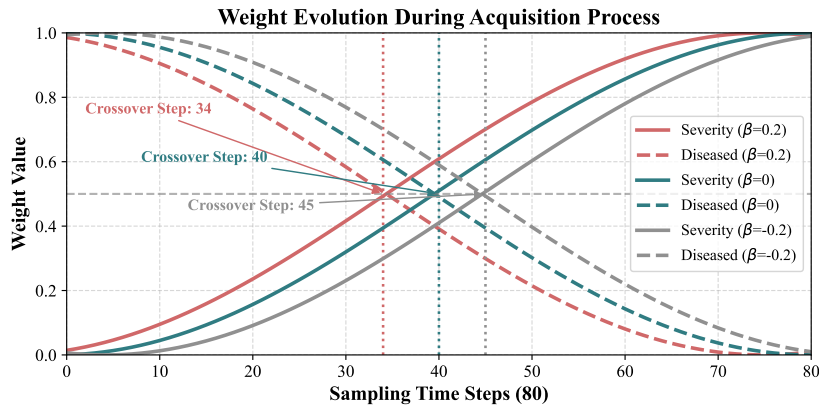


Figure 3: Step-wise weighting evolution for multi-objective diagnosis following lexicographic ordering. The step-wise weight dynamically determines the preference of the reward feedback in disease detection and severity quantification objectives, which ensures a smooth transition. Different β values enable different transition patterns, which can be adjusted based on optimized objectives .

Table 2: Train-Val-Test Split for ACL Sprain and Cartilage Thickness Loss datasets

Pathology	ACL Sprain			Cartilage Thickness Loss		
Severity Degree	No Finding	Low-Mod Grade	High Grade	No Finding	Partial	Full
Train	30915	617	503	29768	1850	417
Validation	5180	56	58	4907	325	62
Test	1734	42	65	1732	79	30
Total	37829	715	626	36407	2254	509

4. Experimental Setup

4.1. Dataset and Pre-processing

Dataset: Experiments are conducted with the single-coil k -space data and slice-level labels from the publicly available fastMRI dataset (Zbontar et al., 2018) and fastMRI+ dataset (Zhao et al., 2022). We use 1,172 annotated volumes from the fastMRI Knee dataset to validate the performance of our framework in two types of pathology diagnosis and severity quantification: *ACL Sprain (High Grade/Low-Moderate Grade)* and *Cartilage Thickness Loss (Full/Partial)*. We follow the data split provided by the dataset, resulting in the distribution of Table 2.

Data Pre-processing: Since the k -space data have varying sizes, we first apply inverse Fourier transform to obtain the fully sampled k -space data to get the ground truth image and crop it to size (320×320) for computational efficiency. After applying Fourier transform to the ground truth image, we

obtain the ground truth k -space data. There is a severe class imbalance between the two diagnostic tasks. To address it during training, we use weighted cross-entropy loss based on the label distribution to avoid overfitting to the majority class and poor generalization on the minority class. When training the policy network, we undersample the data for computational savings, as suggested in (Bakker et al., 2020; Du et al., 2024).

4.2. Baselines and Benchmarks

We design benchmark methods and baselines based on different diagnostic strengths, data access, and objectives as shown in Table 1, to fairly evaluate our approach.

4.2.1. Fully Sampled Classifier (Oracle)

This serves as an oracle benchmark for classifier performance with fully sampled k -space data as input, and hence no sampling optimization occurs. We trained the disease classifier with the ground truth spatial images \mathbf{I} which are derived from fully sampled k -space data and supervised by the disease level label. The severity classifier is fine-tuned from the well-trained disease classifier with only diseased subjects and their severity label. The sequential diagnosis results are inferred by connecting disease and severity classifiers together. We refer to it as *Fully Sampled*.

4.2.2. Undersampled Classifier

The classifier serves as a baseline for single binary tasks, such as disease diagnosis and severity quantification, with spatial representation \mathbf{SR} which derived from the randomly undersampled k -space data and no sampling optimization. It adopts the same backbone as the *Oracle* and is trained with undersampled representations following Variable Density Sampling with various sample rates (5% to 30%) and center fraction (0% to 5%), supervised as before. We refer to it as *Undersampled*.

4.2.3. Single-task Oriented Methods

The methods introduced here are designed for single-task evaluation, targeting binary diagnosis of disease detection or severity quantification.

Policy Classifier (Du et al., 2024): This diagnosis-oriented policy benchmark optimizes patient-level sampling in k -space for direct inference without reconstruction, setting the upper bound for disease detection and severity

quantification. For disease detection, we use a backbone similar to *Under-sampled* as a pre-trained classifier. For severity quantification, the classifier is fine-tuned from the disease detection model. Sampling policy rewards are computed via weighted cross-entropy predictions, with feature maps from the pre-trained classifier as input to the policy network. Training starts with a 5% initial sample rate following Variable Density Sampling, progressively sampling 80 lines to reach a 30% budget.

Policy (via) Reconstruction (Bakker et al., 2020): This model optimizes patient-level sampling with image reconstruction error as rewards, providing a comparison when reconstruction is involved in diagnosis. We pre-train a U-Net (Ronneberger et al., 2015) with a 16-channel first feature map and 4 pooling cascades, totaling 837K parameters. The model is trained across sampling rates (5%–30%) with a 5% center fraction using Variable Density Sampling, supervised using ℓ_1 loss. The active sampler, built on the reconstruction model, uses reconstructed images as input and optimizes sampling with SSIM (Wang et al., 2004) as the reward. This cascaded design totals 26.7M parameters. Its diagnostic evaluation adopts the *Oracle* classifiers, which are trained to make predictions from fully sampled spatial images, leading to the Policy-based Reconstruction Network (*Policy Recon*).

4.2.4. Multi-task oriented Methods for Comprehensive Diagnosis

These diagnosis-oriented methods are designed for multi-task evaluation, aiming to provide a comprehensive diagnosis of the presence and severity of disease. These methods do not consider the order of objectives and enforce sequential steps.

Simulated Policy Classifier: This benchmark evaluates a single-objective reinforcement learning (SORL) policy network tailored for comprehensive diagnosis. It adopts a similar architecture to our framework, e.g., extracting the high-level features from the pre-trained disease and severity classifiers, while using a different rewarding mechanism. Instead of relying on step-wise weighting to adjust the diagnostic rewards, this policy is optimized via a reward function that unifies the diagnostic outcomes as the F1-score of a three-class classification task, where the final diagnosis is categorized as: (0) no findings, (1) diseased with low severity, and (2) diseased with high severity. This formulation simulates the situation where the model simultaneously infers both the presence and severity of disease, without enforcing sequential steps. We refer to this approach as *Simulated Policy*.

Varying Parameter Policy Classifier: To benchmark diagnosis using

multi-objective reinforcement learning (MORL) without specifying the optimization order of objectives, we introduce a method based on the varying parameter approach (Liu et al., 2014). This method employs two separate policy networks—one for disease detection and another for severity quantification—designing sampling trajectories independently before averaging their outputs to guide k -space selection. Each policy is trained with its individual reward, but during joint training, the severity policy considers rewards only from diseased subjects, ignoring others. This approach is termed *Varying Parameter Policy*.

4.2.5. *Weighted Sequential Policy Classifier (Ours)*

Our proposed method, introduced in Section 3 is a MORL-based policy network coupled with a step-wise weighting mechanism. The pre-trained disease classifier shares the same backbone as *Undersampled* and only has access to undersampled k -space data. The severity classifier is fine-tuned from the well-trained disease classifier. Both classifiers are utilized to provide step-wise weighting rewards and high-level feature representations to the policy network as illustrated in Figure 2. During joint training, only when the input subject is diseased does the severity reward from the classifier get used. Our method is referred to as *Weighted Policy*.

To establish a direct baseline for our method, we include the *Random Policy*. This baseline utilizes a randomly initialized network identical in architecture to the *Weighted Policy* to provide unguided, stochastic selection for the next sampling location.

4.3. *Evaluation Metrics*

To assess diagnostic performance, we evaluate our method from three perspectives: disease detection, severity quantification, and overall sequential diagnosis, using **Area Under the Receiver Operating Characteristic Curve (AUC)** and **Balanced Accuracy** as primary metrics. For disease detection, we assess the model’s ability to distinguish pathological cases from no findings. Severity quantification focuses on positive cases, evaluating accuracy in classifying disease progression (Low-Moderate vs. High Grade for ACL Sprain; Partial vs. Full for Cartilage Thickness Loss). Sequential diagnosis treats the process as trajectory prediction, requiring correct classification at both stages—detecting disease and assessing severity—for a prediction to be valid, aligning with real-world clinical needs. Addition-

ally, sampling and computational efficiency metrics have been included for a comprehensive evaluation.

Beyond standard diagnostic performance, we incorporate four metrics that specifically address clinical risk and patient safety across the diagnostic pipeline. For disease detection, we focus on the risks associated with false negatives. The **disease detection missed rate** evaluates the proportion of diseased subjects misclassified as healthy, a critical error that can delay necessary treatment. Building on this, we specifically isolate the number of **missed high-severity subjects**. This metric highlights a subset of patients for whom a missed diagnosis introduces significantly higher clinical risk. For severity quantification stage, we examine misclassification errors among diagnosed patients. We first assess **low-severity overestimation rate**, where incorrectly escalating the severity level may lead to wasted medical resources. Conversely, we track **high-severity underestimation rate**, an error that carries the dangerous consequence of potential undertreatment.

4.4. Implementation Details

All classification networks employed share the same ResNet-50 (He et al., 2016) backbone with 25.6M parameters. To avoid overfitting caused by class imbalance, a dropout layer is added at the end, and weighted cross-entropy is used as the supervised learning loss (Mao et al., 2023). For methods involving a policy with greedy actions, we use the policy gradient network (11M parameters) (Du et al., 2024; Bakker et al., 2020) with parallel acquisition $q = 8$. The network consists of convolutional feature extraction layers with instance normalization followed by a three-layer fully connected head that outputs action logits for k -space line selection. For all methods, we employ the Adam optimizer (Kingma and Ba, 2014) with a learning rate of 10^{-4} and a step-based scheduler with a decay gamma of 0.1 for all model training. All disease classification and reconstruction models are trained for 50 epochs, and the severity classification model is fine-tuned for 20 epochs. For the policy model, we train it for 30 epochs. Our experimental setup uses the PyTorch framework, and all computations are performed on an NVIDIA A100 Tensor Core GPU. Our code is publicly available at https://github.com/vios-s/MRI_Sequential_Active_Sampling.

Table 3: Average balanced accuracy (%) and Area Under Curve (%) results and the standard deviations of different diagnostic policies across varying sampling rates for ACL Sprain Diagnosis. Dashes (—) indicate scenarios where the method is not applicable. Bold numbers denote the best performance

Diagnosis Task	Balanced Accuracy ↑					Severity Degree					Sequential Diagnosis				
	Disease					Disease					Disease				
Fully Sampled (Oracle)	84.27 _{6,0}					69.20 _{1,5}					65.94 _{6,1}				
Sampling Rate	5%	10%	15%	20%	30%	5%	10%	15%	20%	30%	5%	10%	15%	20%	30%
Undersampled	72.90 _{2,9}	75.68 _{2,5}	76.14 _{1,9}	76.58 _{1,8}	79.64 _{0,8}	60.62 _{1,7}	61.20 _{3,0}	62.90 _{3,1}	64.58 _{4,0}	68.42 _{2,5}	—	—	—	—	—
Policy Classifier (Du et al., 2024)	72.90 _{2,9}	81.32 _{1,7}	81.78 _{1,4}	81.84 _{0,7}	82.94 _{0,8}	60.62 _{1,7}	71.94 _{2,7}	74.08 _{2,3}	74.64 _{1,9}	78.58 _{2,6}	—	—	—	—	—
Policy Recon (Bakker et al., 2020)	62.54 _{0,1}	69.60 _{0,4}	78.60 _{0,4}	79.14 _{0,2}	81.92 _{0,5}	37.70 _{0,0}	30.32 _{1,9}	43.08 _{2,7}	49.14 _{0,1}	54.64 _{2,1}	41.90 _{0,0}	39.68 _{0,7}	52.44 _{1,7}	55.22 _{0,1}	60.40 _{1,1}
Random Policy	73.26 _{2,8}	75.02 _{2,6}	76.54 _{2,9}	77.48 _{1,9}	79.30 _{1,2}	58.94 _{4,1}	62.90 _{2,2}	61.46 _{2,2}	64.68 _{1,8}	66.32 _{2,0}	53.58 _{3,1}	56.00 _{3,4}	56.32 _{1,8}	59.64 _{1,9}	61.80 _{1,4}
Weighted Policy (Ours)	73.26 _{2,8}	84.20 _{3,3}	84.76 _{1,0}	84.34 _{0,7}	83.54 _{0,4}	58.94 _{4,1}	76.86 _{2,8}	74.10 _{3,1}	73.88 _{1,9}	75.36 _{2,8}	53.58 _{3,1}	73.42 _{2,0}	72.36 _{1,9}	71.72 _{1,7}	71.68 _{1,6}
Area Under Curve ↑															
Fully Sampled (Oracle)	90.23 _{3,0}					71.03 _{1,2}					80.76 _{6,1}				
Sampling Rate	5%	10%	15%	20%	30%	5%	10%	15%	20%	30%	5%	10%	15%	20%	30%
Undersampled	84.10 _{1,8}	85.58 _{1,3}	86.50 _{1,2}	87.28 _{1,3}	88.40 _{0,7}	69.20 _{4,6}	70.34 _{5,5}	73.38 _{4,5}	75.36 _{4,2}	79.70 _{4,7}	—	—	—	—	—
Policy Classifier (Du et al., 2024)	84.10 _{1,8}	88.72 _{0,5}	88.64 _{0,5}	88.54 _{0,4}	88.98 _{0,4}	69.20 _{4,6}	83.78 _{1,7}	84.80 _{1,3}	85.10 _{1,4}	87.16 _{1,5}	—	—	—	—	—
Policy Recon (Bakker et al., 2020)	78.16 _{1,1}	84.02 _{0,1}	87.98 _{0,0}	88.44 _{0,1}	89.30 _{0,1}	35.80 _{0,0}	25.40 _{0,5}	42.10 _{0,9}	46.66 _{0,4}	57.86 _{0,9}	56.98 _{0,0}	54.72 _{0,3}	65.02 _{0,4}	67.56 _{0,2}	73.58 _{0,4}
Random Policy	83.24 _{1,5}	84.98 _{0,7}	85.98 _{0,9}	86.72 _{0,8}	87.98 _{0,7}	67.22 _{5,5}	72.06 _{4,6}	73.16 _{3,8}	74.52 _{3,2}	77.02 _{2,7}	75.22 _{3,0}	78.52 _{2,2}	79.54 _{1,8}	80.62 _{1,8}	82.50 _{1,6}
Weighted Policy (Ours)	83.24 _{1,5}	89.32 _{4,4}	89.54 _{2,2}	89.50 _{0,1}	89.36 _{0,3}	67.22 _{5,5}	88.14 _{1,2}	86.76 _{1,4}	86.08 _{1,0}	87.44 _{1,1}	75.22 _{3,0}	88.72 _{0,6}	88.14 _{0,8}	87.78 _{0,5}	88.40 _{0,7}

Table 4: Same as in Table 3 but for Cartilage Thickness Loss

Diagnosis Task	Balanced Accuracy ↑					Severity Degree					Sequential Diagnosis				
	Disease					Disease					Disease				
Fully Sampled (Oracle)	75.05 _{6,1}					60.90 _{2,7}					54.84 _{4,0}				
Sampling Rate	5%	10%	15%	20%	30%	5%	10%	15%	20%	30%	5%	10%	15%	20%	30%
Undersampled	71.12 _{4,0}	73.22 _{2,2}	74.32 _{2,9}	74.62 _{1,4}	75.22 _{1,4}	54.90 _{2,3}	59.42 _{2,0}	59.02 _{2,0}	60.32 _{2,3}	61.38 _{2,8}	—	—	—	—	—
Policy Classifier (Du et al., 2024)	71.12 _{4,0}	73.72 _{2,5}	75.14 _{1,1}	75.30 _{1,3}	75.98 _{1,2}	54.90 _{2,3}	58.58 _{4,0}	60.30 _{4,4}	63.10 _{3,9}	63.84 _{4,0}	—	—	—	—	—
Policy Recon (Bakker et al., 2020)	64.34 _{0,1}	65.86 _{0,9}	72.18 _{0,3}	71.20 _{0,3}	75.92 _{0,4}	56.58 _{0,0}	56.98 _{1,0}	54.50 _{0,9}	55.18 _{0,0}	56.60 _{0,9}	45.22 _{0,0}	44.72 _{1,3}	50.18 _{0,7}	50.16 _{0,1}	54.46 _{0,7}
Random Policy	72.76 _{1,5}	73.88 _{1,6}	75.08 _{0,8}	75.20 _{1,3}	76.06 _{1,8}	58.92 _{5,7}	61.66 _{6,8}	61.60 _{4,8}	62.22 _{2,9}	63.64 _{3,9}	54.40 _{2,8}	54.66 _{1,2}	55.64 _{1,9}	55.80 _{1,9}	58.44 _{2,9}
Weighted Policy (Ours)	72.76 _{1,5}	72.96 _{1,0}	74.02 _{0,9}	73.86 _{1,1}	73.84 _{1,5}	58.92 _{5,7}	60.62 _{3,9}	58.98 _{2,8}	60.88 _{3,5}	62.32 _{3,0}	54.40 _{2,8}	54.88 _{2,1}	53.90 _{2,2}	54.80 _{0,9}	55.48 _{0,6}
Area Under Curve ↑															
Fully Sampled (Oracle)	88.23 _{3,0}					73.58 _{4,2}					80.88 _{6,5}				
Sampling Rate	5%	10%	15%	20%	30%	5%	10%	15%	20%	30%	5%	10%	15%	20%	30%
Undersampled	84.58 _{1,0}	86.02 _{0,7}	87.38 _{0,3}	87.86 _{0,7}	88.08 _{0,6}	61.90 _{0,0}	66.40 _{1,4}	68.76 _{3,3}	71.80 _{4,4}	76.82 _{4,5}	—	—	—	—	—
Policy Classifier (Du et al., 2024)	84.58 _{1,0}	86.74 _{0,4}	87.32 _{0,4}	87.82 _{0,4}	87.96 _{0,4}	61.90 _{0,0}	81.12 _{2,0}	83.10 _{1,6}	83.24 _{1,3}	85.26 _{1,4}	—	—	—	—	—
Policy Recon (Bakker et al., 2020)	83.72 _{0,0}	85.30 _{0,1}	86.18 _{0,1}	86.42 _{0,0}	87.38 _{0,1}	71.44 _{0,1}	68.32 _{0,9}	71.30 _{0,6}	70.52 _{0,6}	75.00 _{0,9}	77.58 _{0,0}	76.84 _{0,4}	78.74 _{0,3}	78.48 _{0,3}	81.22 _{0,4}
Random Policy	85.24 _{0,8}	86.18 _{1,0}	86.98 _{0,3}	87.52 _{0,6}	88.44 _{0,9}	65.72 _{1,1}	70.28 _{0,0}	71.04 _{0,6}	75.54 _{1,7}	78.52 _{2,9}	75.46 _{3,2}	78.20 _{2,7}	79.00 _{2,6}	81.54 _{2,4}	83.48 _{1,5}
Weighted Policy (Ours)	85.24 _{0,8}	87.34 _{0,3}	89.06 _{0,4}	88.98 _{0,3}	89.02 _{0,3}	65.70 _{1,1}	75.04 _{1,2}	80.94 _{1,6}	83.60 _{1,0}	85.58 _{1,5}	75.44 _{3,2}	81.20 _{0,6}	84.98 _{0,8}	86.28 _{0,6}	87.26 _{0,8}

5. Experimental Results and Analysis

We divide this section into several parts, each addressing key questions or hypotheses. First, we aim to show that our approach maintains diagnostic performance when compared to other non-sequential and single objective policies. We then proceed to address our main hypothesis that adopting sequential decisions leads to k -space savings. Finally, we show that the natural ordering of the objectives results in even more savings.

5.1. Comparison to Non-sequential and Single Objective Policies

In this section, we first answer a critical question: *Will our method compromise performance when enforcing multiple objectives in a single scan?* We compare the performance of our sequential diagnosis method with baselines and benchmarks designed for a single binary diagnosis task, namely the *Undersampled*, *Policy Recon*, and *Policy Classifier*, at various sample rates for inferring the conditions of ACL Sprain and Cartilage Thickness Loss. *Undersampled* randomly samples k -space lines progressively. *Policy Recon*, *Policy Classifier*, and *Weighted Policy* start with a randomly initialized mask at a sample rate of 5% and perform sampling decision-making respectively using their policies (see Section 4.2). We also include *Fully sampled* as a diagnostic oracle, which does not have a sampling budget. Additionally, *Random Policy* is included as the direct baseline for *Weighted Policy*, which provide random guidance. The results are shown in Table 3 and Table 4.

Our *Weighted Policy*, consistently demonstrates strong performance in all metrics across different sampling rates and both tasks (ACL Sprain and Thickness Loss). Focusing first on Table 3, we observe that: (i) *Weighted Policy* approaches the performance of *Fully Sampled*, showing that careful selection of k -space lines avoids taking redundant and irrelevant information. (ii) The advantage of policy-based optimization in our method is clearly demonstrated as we can approach the performance of *Fully Sampled* with roughly 10% k -space data across all subtasks. (iii) As expected, *Policy Recon*, although providing benchmark reconstruction performance as described in (Bakker et al., 2020), underperforms our approach, which optimizes for each task at hand. (iv) More importantly, our *Weighted Policy*, which jointly optimizes disease detection and severity quantification, outperforms the *Policy Classifier* in most cases even when used for a single subtask with fewer samples. In fact, with 10% sampling in disease detection (84.20% vs. 81.32%) and 20% k -space sampling for severity quantification (74.10% vs. 74.08%),

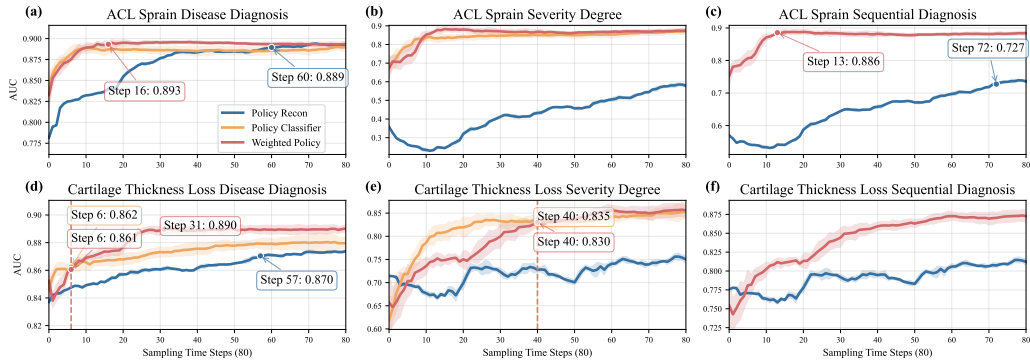


Figure 4: Performance comparison of our proposed *Weighted Policy* and two single-task oriented policies. The horizontal axis indicates the cumulative lines acquired when sampling. The 80-step active sampling procedure starts from 16 randomly sampled k -space lines. Earlier plateau indicates fewer required k -space lines.

this finding is extremely important, as it answers the initially posed question. It demonstrates that a policy optimized for multiple objectives does not compromise diagnostic performance compared to policies optimized for a single objective.

Similar observations hold for Cartilage Thickness Loss in Table 4, evidently illustrating the applicability of our methods in two settings and hence the strength of our findings.

5.2. k -space Savings

We now proceed to answer our main hypothesis: *Joint optimization of a policy for two objectives ultimately leads to sampling efficiency and savings.*

In Figure 4, we illustrate the diagnostic performance of policies that progressively make decisions on which line to acquire, line-by-line, and visualize their sampling trajectories. We present the performance of our method and compare with *Policy Recon* and *Policy Classifier* to showcase the difference between sampling patterns of single-task methods versus ours.

We find that the performance curve plateaus during the sampling process, indicating that the policies might have collected the majority of diagnostically significant k -space lines that contribute to diagnostic performance enhancement.

For disease detection, as shown in Figure 4 (a) and (d), compared to *Policy Recon* which optimizes sampling trajectories for reconstruction, our method plateaus earlier at step 16 for ACL Sprain, whereas *Policy Recon*

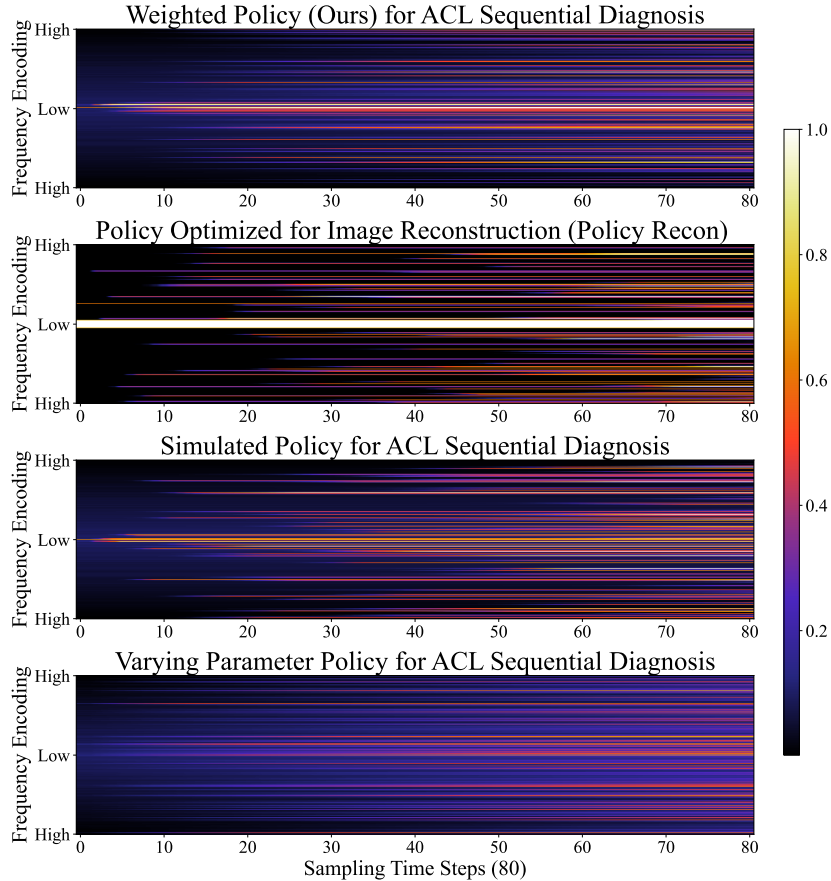


Figure 5: Average k -space sampling behaviors across all subjects of our proposed *Weighted Policy* and benchmarks. A High value in the plot represents a high probability to be sampled. The horizontal axis indicates the cumulative lines acquired when sampling.

plateaus much later (at step 60 for ACL Sprain leading to considerable k -space savings. The advantage of a diagnosis-oriented policy is further highlighted in severity quantification (Figure 4 (b)), where our method successfully identifies k -space lines that can significantly improve inference. In contrast, although it can achieve continuous improvements in reconstruction performance, *Policy Recon* struggles to effectively locate diagnostically relevant k -space lines and produce comparable outcomes in both severity and sequential diagnosis classification. Consequently, when evaluating sequential diagnosis in ACL Sprain (Figure 4 (c)), our method reaches a plateau at step 13 with a high AUC of 0.886, while *Policy Recon* arrives at step 72 with

Table 5: Sampling and Computational Efficiency Metrics evaluated on a single NVIDIA A100 Tensor Core GPU. n/a refers to non applicable.

Method	Policy Classifier (Du et al., 2024)	Policy Recon (Bakker et al., 2020)	Weighted Policy (Ours)
<i>Sampling Efficiency</i>			
Initial 5% Acquisition (ms)	20.00	20.00	20.00
Selection Time (ms/step)	14.33	29.67	26.53
<i>Computational Efficiency</i>			
Inference Time (ms)	12.62	29.93	25.31
Reconstruction Time (ms)	n/a	3.73	n/a
Total Pipeline Latency (ms)	12.62	33.66	25.31
Peak Memory Usage (GB)	0.58	1.19	1.11

the AUC of 0.727. Similar observations hold for Cartilage Thickness Loss (Figure 4 (d) to (f)).

In Figure 4, compared to the policies of *Policy Classifier* that optimize sampling trajectories independently for separate tasks (disease detection or severity quantification), our method provides competitive results and achieves considerable acquisition savings. For ACL Sprain, our policy quickly approaches the performance of *Policy Classifiers*, and exceeds them afterward. Similarly, as shown in plots (d) and (e), *Weighted Policy* samples 6 lines in disease detection and 40 lines in severity quantification for Cartilage Thickness Loss to achieve the performance of the corresponding *Policy Classifier*. Notably, our policy achieves this sequentially whereas the other policies require different sessions for two tasks. Hence, our method can significantly reduce the quantity of necessary k -space lines and thereby shorten the acquisition time.

Sampling efficiency and inference latency are critical for clinical viability. As reported in Table 5, the initial 5% acquisition requires 20 ms, and the policy requires 26.53 ms per subsequent k -space line selection for the proposed method and 4.62 ms more for *Policy Recon*. In ACL sprain sequential diagnosis, performance plateaus at step 13 for the proposed method versus step 72 for *Policy Recon*, corresponding to a 1791.35 ms reduction in total sampling time. Compared to the *Policy Recon*, our method achieves additional savings by eliminating reconstruction (3.73 ms) and performing direct k -space inference (29.93 ms versus 25.31 ms). Notably, if we consider a "trigger" system with two separate *Policy Classifiers* for two objectives, which requires re-initiating the sampling protocol upon positive disease identification, the system incurs supplementary overhead comprising initial 5% acquisition time (20 ms) and extended k -space line selection (33.29 ms). Collectively, such computational efficiencies reduce acquisition time without compromising diagnostic accuracy, and translate into even more substantial time savings

during practical MRI acquisition. Consider a typical Fast Spin Echo (FSE) sequence with a repetition time (TR) of 2000 ms and an Echo Train Length of 4, encoding four k -space lines per TR. Following a universal 4-TR initial sampling phase, existing approaches require significantly more scan time: A “trigger” system including two *Policy Classifiers* needs 25 lines (15 for disease identification and 10 for severity quantification), requiring 15 TRs (including re-initiation) for 30,000 ms, while the *Policy Recon* baseline requires 72 lines, necessitating 22 TRs for 44,000 ms. In contrast, our method achieves its diagnostic goal in just 13 steps, requiring only 8TRs and 16,000 ms of scan time. This yields time savings of 14,000 ms compared to the *Policy Classifier* and 28,000 ms compared to *Policy Recon*, demonstrating how our method reduces the actual time patients spend in the scanner—a critical advantage for clinical viability.

Additionally, we want to compare the sampling behaviors of different policies averaged across the subject population. As shown in Figure 5, referring to the top two plots, there are evident differences between the trajectories of *Policy Recon* and *Weighted Policy*. *Policy Recon* tends to consistently sample low-frequency central k -space lines, whereas our method shows a broader diversity (across the frequency spectrum), illustrating its adaptation at the patient level.

5.3. Sequential Diagnosis in One Scanning Session

We base our work on a key question: *Is it necessary to adopt a sequential process, detecting disease first and then assessing severity?* This question is crucial because our proposed sequential diagnosis workflow employs the lexicographic ordering in step-wise weighting module, attempting to mirror the clinical workflow of radiologists. To address this key question, we train two policies with different ways to optimize for multiple objectives in parallel and independently. The first, termed *Simulated Policy*, uses the same architecture as ours but employs a single-objective RL algorithm rewarded by the performance of a three-way diagnosis (no finding, low, or high severity) without specifying the lexicographic ordering among diagnostic objectives. The second, the *Varying Parameter Policy*, is instead a MORL-based method, which uses separate policies to optimize detection and quantification in parallel as independent objectives, and the final sampling policy is the average of the result of the two policy networks.

Referring to Figure 6 and first focusing on comparisons with the *Simulated Policy*, we see that the *Simulated Policy* plateaus earlier at a lower

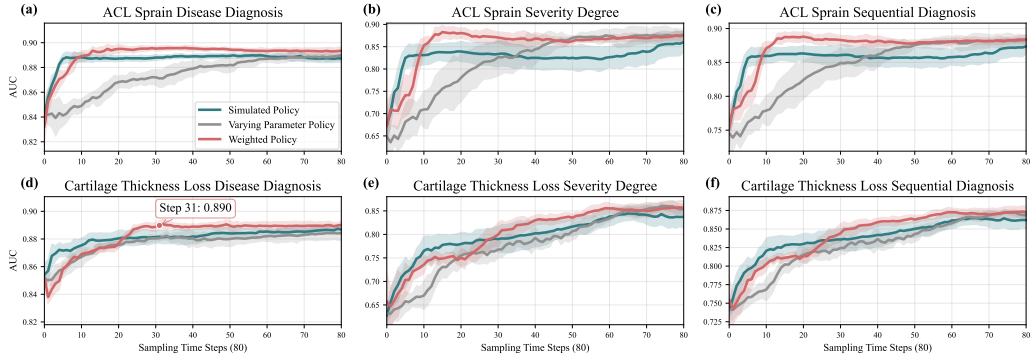


Figure 6: Performance comparison of our proposed *Weighted Policy* and two multi-task oriented policies. The horizontal axis indicates the cumulative lines acquired when sampling. The 80-step active sampling procedure starts from 16 randomly sampled k -space lines. Earlier plateau indicates fewer required k -space lines.

performance compared to our method. This is because the *Simulated Policy* is rewarded based on overall sequential diagnosis improvements, forcing the policy to find k -space lines that contribute to a three-way objective, therefore lacking reward information for each independent objective. Our method explicitly calculates the separate rewards of the two objectives, which simplifies the sequential diagnosis task and reduces the complexity of the sampling strategy optimization.

We compare with *Varying Parameter Policy*, a MORL-based trained policy, whose key differences are: (i) it employs individual policies to process rewards from the independent objectives in parallel; and most importantly, (ii) it does not utilize the lexicographic ordering between objectives. Thus, we expect to observe worse performance for this ‘simpler’ policy. Looking again at Figure 6, and now comparing the ‘grey’ (*Varying Parameter Policy*) and ‘red’ (*Weighted Policy*) lines, our method outperforms the other policy and plateaus earlier at a higher accuracy level, particularly in the overall sequential diagnosis (Figure 6 (c) and (f)), hence achieving k -space sampling savings and in turn less scanning time. This highlights the benefits of lexicographic ordering in multi-objective optimization and step-wise weighting. Our policy thus learns the inherent shared diagnostic features between disease detection and severity quantification, and is encouraged to seek mutually beneficial lines during sampling. Consequently, in Figure 6 Cartilage Thickness Loss, after sampling what is needed to decide in the presence of

Table 6: Performance comparison of *Weighted Policy* against *Fully Sampled (Oracle)* baseline across different sampling rate. Δ shown in parentheses indicate change from Oracle baseline. The Initial 5% samples are randomly sampled.

Sampling Rate	Disease Miss Rate (%) \downarrow	High Grade Missed (n) \downarrow	Severity Overestimation (%) \downarrow	Severity Underestimation (%) \downarrow
<i>Fully sampled (Oracle)</i>				
100%	14.04	7	20.59	42.91
<i>Weighted Policy (Ours)</i>				
5%	37.83 (+23.8)	29.4 (+22.4)	16.13 (-4.5)	73.45 (+30.5)
10%	15.73 (+1.7)	11.6 (+4.6)	4.89 (-15.7)	35.71 (-7.2)
15%	15.92 (+1.9)	11.4 (+4.4)	7.69 (-12.9)	37.45 (-5.5)
20%	17.04 (+3.0)	12.8 (+5.8)	8.74 (-11.9)	37.69 (-5.2)
30%	18.54 (+4.5)	13.8 (+6.8)	7.78 (-12.8)	36.08 (-6.8)

disease (shown as plateauing at step 31 subplot (d), the optimization prioritizes sampling of k -space lines that contribute to severity as observed by an increase in performance in the subplot (e) without compromising disease diagnosis performance (the plateau).

We can observe such transitions also at the level of sampling trajectories in Figure 5 as well. Looking at the bottom two plots and comparing them with the topmost, until sampling step 16, our proposed policy samples more low-frequency lines (containing structural information) that can contribute to both objectives and patient-level disease-related information (shown as purple in the plot). Then, the policy smoothly shifts to sampling diagnostic features located in high-frequency zone, which may contribute to severity quantification for ACL Sprain. While *Varying Parameter Policy* tends to find patient-level features from the start, it can miss the mutual diagnostically significant lines between disease detection and severity quantification. The probability trajectories of the *Simulated Policy* show several frequency locations with high sampling probability, illustrating a tendency to generate similar sampling trajectories for all subjects, thereby lacking exploration of patient-level diagnostic information.

5.4. Diagnostic Risk and Safety Evaluation

In this section, we investigate the diagnostic risk and safety of **Weighted Policy** for ACL sprain diagnosis, in comparison with **Fully Sampled (Oracle)** as summarized in Table 6. The critical clinical risk is missed detection (false negatives), which delays diagnosis and appropriate treatment (Arastu et al., 2015). The disease miss rate demonstrates that our method can effectively approach the performance of the *Fully Sampled* baseline with only 10% sampling, achieving a disease miss rate of 15.73% compared to 14.04% for the oracle (+1.7 %). We also evaluate how many patients with high-grade ACL tears are missed during detection. At 10% sampling, our method misses

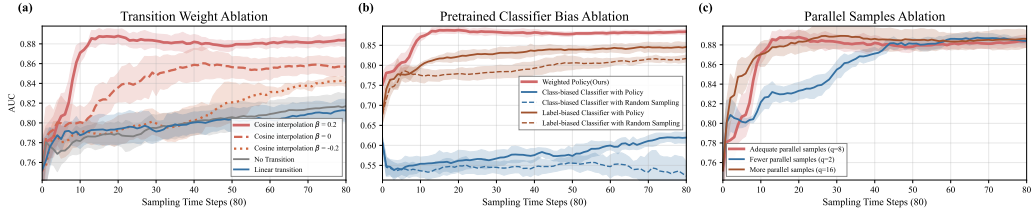


Figure 7: Ablation studies on ACL sprain diagnosis. We evaluate the sensitivity of our framework to (a) different transition weight strategies, (b) biases in the pretrained classifier, and (c) the number of parallel samples acquired during training.

11.6 high-grade cases compared to 7 for *Fully Sampled*, representing an increase of 4.6 cases. This modest increase must be interpreted in the context of reduced acquisition time and may have different implications depending on the clinical setting.

Regarding severity assessment errors, our **Weighted Policy** exhibits surprising characteristics. Severity overestimation rate decreases substantially compared to the oracle baseline across all sampling rates, with the most pronounced reduction at 10% sampling (4.89% vs. 20.59%, $\Delta = -15.7$). Similarly, Weighted Policy outperforms oracle performance in Severity underestimation rate at 10% sampling (35.71%, $\Delta = -7.2$). The superiority in severity estimation proving its diagnostic safety while enabling substantial savings in medical resources and appropriate healthcare to each patient.

Overall, the **Weighted Policy** at 10% sampling demonstrates a positive performance-efficiency trade-off, maintaining disease detection performance comparable to *Fully Sampled* while substantially reducing acquisition time. The observed increase in high-grade missed cases (4.6 additional cases) should be interpreted in the context of faster scanning, which contributes to improved patient comfort, reduced motion artifacts, and increased throughput.

6. Ablation Studies

To validate our model design choices and assess the sensitivity of our framework to key hyperparameters, we conduct comprehensive ablation studies on ACL sprain diagnosis. We analyze three critical components: (a) Transition Weight (b) Pretrained Classifier Bias and (c) Parallel Samples, summarized in Figure 7, provide insights into the robustness and design rationale of our approach.

6.1. Sensitivity to Step-wise Transition Weight

We investigate five different transition strategies for balancing disease detection and severity quantification rewards during the sampling process. As shown in Figure 7(a), the policy without any transition mechanism, which we assign equal weight to both objectives, performs poorly, demonstrating the necessity of structured reward scheduling with lexicographic ordering. While both linear interpolation and standard cosine interpolation show improvement over the no-transition baseline, our proposed cosine interpolation achieves superior performance compared to linear interpolation by enabling adaptive and customized transition as shown in Figure 3 instead of fixed-step transition. For the ACL Sprain diagnosis task, this configuration achieved the highest AUC with $\beta = 0.2$ (early transition at step 34) and demonstrated efficient convergence compared to $\beta = 0$ (transition at step 40) or $\beta = -0.2$ (late transition at step 45). This result may be attributable to the lower relative complexity of detecting disease compared to quantifying its severity. This confirms that a carefully designed transition enhances diagnostic performance and suggests that task-specific transition points could be beneficial, potentially learned as a function of task complexity.

6.2. Sensitivity to Pretrained Classifier Performance

Our framework employs pretrained classifiers as both reward models and inference operators, which may lead to error propagation to the sampling policy. To assess this potential, we conduct sensitivity analysis with two simulated bias conditions: (i) **Class-imbalance bias**: We train classifiers using standard cross-entropy loss instead of the weighted cross-entropy employed in our main approach, simulating scenarios where class imbalance is not properly addressed. (ii) **Label annotation bias**: We randomly flip 10% of severity labels in the training set to simulate human annotation errors commonly encountered in clinical datasets.

As illustrated in Figure 7(b), As illustrated in Figure 7(b), both bias conditions affect policy performance. Label annotation bias results in 7% AUC degradation, as the policy receives noisy reward signals from erroneous severity predictions. Class-imbalance bias leads to a 35% performance decrease, indicating that the policy becomes trapped by the majority class distribution due to the biased reward. Our method still does better than using random sampling.

These findings underscore the critical importance of reward quality in reinforcement learning frameworks, which is widely known in the RL com-

munity. They also demark the criticality of class-imbalance as a worse form of bias, which is expected as this is a consistent bias towards the population vs a random effect (such as label bias). We highlight that the classifier used in our experiments was using bias mitigation strategies precisely for these reasons.

6.3. Sensitivity to Parallel Acquisition Rate

We examine the effect of parallel acquisition number (q) on policy training efficiency and final performance. As shown in Figure 7(c), we compare our chosen setting ($q = 8$) with lower ($q = 2$) and higher ($q = 16$) parallel acquisition rates. With fewer parallel samples ($q = 2$), the policy exhibits slower convergence and plateaus at a later sampling step, matching the performance of $q = 8$ only after extensive sampling. This indicates that insufficient parallel acquisition constrains action space exploration during training, hindering the agent’s ability to efficiently identify diagnostically relevant k -space features. Conversely, with more parallel samples ($q = 16$), the policy achieves slightly earlier plateauing compared to $q = 8$ but does not surpass the final performance level. This suggests that while higher parallel acquisition rates can accelerate the discovery of diagnostic features, they provide diminishing returns beyond an optimal threshold. Our chosen value of $q = 8$ represents an effective balance between exploration efficiency and computational resources.

7. Discussion

7.1. Clinical Relevance

Our framework enables the efficient acquisition of diagnostically relevant k -space data while sequentially performing disease detection and severity quantification in a single scanning session, such as stroke assessment (detecting a bleed first, then quantifying its volume or location) (Greenberg et al., 2022) or acute trauma diagnosis, where a logical, sequential workflow is standard practice (Kool and Blickman, 2007). This approach enables comprehensive assessment during the scanning process, potentially eliminating the need for follow-up examinations. The sequential diagnosis paradigm completes multi-objective diagnostic tasks within a single scanning session without requiring full k -space acquisition, thereby significantly reducing acquisition time.

The acquisition acceleration of the proposed pipeline via patient-level active sampling could substantially enhance the clinical utility of low-field MRI,

making them more viable for PoC applications (Geethanath and Vaughan Jr, 2019). We envision practical implementations in preliminary screening scenarios where rapid assessments are crucial to guide resource allocation decisions (Brady et al., 2021), which is particularly valuable in settings with limited healthcare infrastructure or in emergency medicine contexts (Mazurek et al., 2021) where time-critical diagnostic information is essential.

7.2. Limitations and Future Works

Our method has been implemented as a proof-of-concept on the fastMRI knee dataset, focusing on specific pathologies where k -space data are publicly available with annotated disease and severity labels, proving the feasibility of our method in in-site, rapid assessment. Future work could explore other applications such as stroke (Ho et al., 2019) or acute brain trauma diagnosis (Mazurek et al., 2021), where rapid assessment from limited data is crucial. Although such datasets are not publicly available, we hope our open-source code will encourage researchers with access to evaluate our method in these critical settings.

Methodologically, our approach is tailored to problems with a known and fixed diagnostic sequence, and therefore may not be suitable for clinical scenarios where multiple diagnostic tasks are truly parallel or where the optimal order of tasks is unknown. Future iterations could explore dynamic policies that learn not only *what* to sample but also the optimal *order* of diagnostic objectives. Additionally, while our current hard-gating mechanism is effective for this proof-of-concept, clinical deployment would benefit from more granular uncertainty quantification. Future research could explore uncertainty-aware decision making, where methods like Monte Carlo dropout dynamically modulate the diagnosis threshold, effectively adding a safety layer for ambiguous cases.

A critical area for future improvement is robustness to model bias. As analyzed in Section 6.2, our reliance on pre-trained classifiers can propagate inherent biases and leave the policy vulnerable to domain shift (Wachinger et al., 2021). Nevertheless, our policy-guided sampling can mitigate the bias-induced performance drop compared to random sampling as shown in Figure 7(b), motivating future work on bias-aware policy training. Promising directions include integrating constraints directly into the reward function or employing adversarial debiasing techniques to suppress shortcut attributes (e.g., acquisition site or protocol).

Finally, we acknowledge the hardware constraints associated with practical deployment. The real-time feedback loop required for dynamic, line-by-line trajectory control is not a standard feature on most current mainstream scanners. However, previous works (Contijoch et al., 2020; Liu et al., 2024) demonstrate the feasibility of autonomous, closed-loop k -space trajectory on a clinical MRI scanner with real-time feedback to dynamically update the acquisition sequence. Our research builds on these pioneering efforts, serving as a proof-of-concept to motivate the broader development of programmable acquisition systems that can support intelligent sampling.

8. Conclusion

We propose a novel MORL framework for sequential diagnostic assessment directly from undersampled k -space data. By structuring clinical diagnosis as a sequential decision process with lexicographic ordering, our method achieves diagnostic performance comparable to fully sampled references and outperforms undersampled baselines while significantly reducing acquisition time. Empirical results on two tasks show that our diagnosis-oriented sampling strategy surpasses reconstruction-based methods in both diagnostic accuracy and efficiency. Compared to single-objective diagnostic samplers, our approach achieves substantial k -space savings within a single scan without compromising performance. Our step-wise weighting mechanism effectively prioritizes disease detection early in the acquisition before transitioning to severity assessment, thereby aligning with clinical workflows. Furthermore, the convergence of sampling trajectories across tasks supports the existence of shared informative k -space regions, enabling efficient, comprehensive assessment in a single session. This work advances direct k -space inference, paving the way for clinically viable, PoC MRI diagnostics with reduced acquisition demands.

Declaration of generative AI and AI-assisted technologies in the writing process

During the preparation of this manuscript, the authors utilized Perplexity AI to improve the clarity and flow of the text. The authors reviewed all suggestions and maintain full responsibility for the accuracy and content of the work.

Declaration of competing interest

The authors declare that they have no known competing financial interests or personal relationships that could have appeared to influence the work reported in this paper.

Acknowledgments

This work was supported in part by National Institutes of Health (NIH) grant 7R01HL148788-03. Yuning Du thanks additional financial support from the School of Engineering, the University of Edinburgh. Sotirios A. Tsaftaris acknowledges support from the Royal Academy of Engineering and the Research Chairs and Senior Research Fellowships scheme (grant RC-SRF1819\8\25), and the UK Engineering and Physical Sciences Research Council (EPSRC) support via grant EP/X017680/1, and the UKRI AI programme, Causality in Healthcare AI Hub (CHAI, grant EP/Y028856/1).

References

- Aggarwal, H.K., Jacob, M., 2020. J-modl: Joint model-based deep learning for optimized sampling and reconstruction. *IEEE journal of selected topics in signal processing* 14, 1151–1162.
- Alkan, C., Mardani, M., Vasanaawala, S., Pauly, J.M., 2020. Learning to sample mri via variational information maximization, in: *NeurIPS 2020 Workshop on Deep Learning and Inverse Problems*.
- Anzai, Y., Moy, L., 2022. Point-of-care low-field-strength mri is moving beyond the hype.
- Arastu, M., Grange, S., Twyman, R., 2015. Prevalence and consequences of delayed diagnosis of anterior cruciate ligament ruptures. *Knee Surgery, Sports Traumatology, Arthroscopy* 23, 1201–1205.
- Ayde, R., Vornehm, M., Zhao, Y., Knoll, F., Wu, E., Sarracanie, M., 2025. Mri at low-field:: a review of software solutions for improving snr. *NMR in Biomedicine* 38. doi:10.1002/nbm.5268. open access via the JISC Hybrid CY24 - University of Aberdeen.

- Bahadir, C.D., Wang, A.Q., Dalca, A.V., Sabuncu, M.R., 2020. Deep-learning-based optimization of the under-sampling pattern in mri. *IEEE Transactions on Computational Imaging* 6, 1139–1152.
- Bakker, T., van Hoof, H., Welling, M., 2020. Experimental design for MRI by greedy policy search. *Advances in Neural Information Processing Systems* 33, 18954–18966.
- Brady, A.P., Bello, J.A., Derchi, L.E., Fuchsjäger, M., Goergen, S., Krestin, G.P., Lee, E.J., Levin, D.C., Pressacco, J., Rao, V.M., et al., 2021. Radiology in the era of value-based healthcare: a multi-society expert statement from the acr, car, esr, is3r, ranzcr, and rsna. *Canadian Association of Radiologists Journal* 72, 208–214.
- Chaithya, G., Ramzi, Z., Ciuciu, P., 2022. Hybrid learning of non-cartesian k-space trajectory and mr image reconstruction networks, in: *2022 IEEE 19th International Symposium on Biomedical Imaging (ISBI)*, IEEE. pp. 1–5.
- Contijoch, F., Han, Y., Iyer, S.K., Kellman, P., Gualtieri, G., Elliott, M.A., Berisha, S., Gorman, J.H., Gorman, R.C., Pilla, J.J., Witschey, W.R.T., 2020. Closed-loop control of k-space sampling via physiologic feedback for cine mri. *PLOS ONE* 15, e0244286. URL: <https://app.dimensions.ai/details/publication/pub.1134187574>, doi:10.1371/journal.pone.0244286. <https://escholarship.org/uc/item/4df7806k>.
- Du, Y., Dharmakumar, R., Tsaftaris, S.A., 2024. The MRI scanner as a diagnostic: image-less active sampling, in: *International Conference on Medical Image Computing and Computer-Assisted Intervention*, Springer. pp. 467–476.
- Geethanath, S., Vaughan Jr, J.T., 2019. Accessible magnetic resonance imaging: a review. *Journal of Magnetic Resonance Imaging* 49, e65–e77.
- Greenberg, S., Ziai, W., Cordonnier, C., Dowlatshahi, D., Francis, B., Goldstein, J., Hemphill, J., Johnson, R., Keigher, K., Mack, W., Mocco, J., Newton, E., Ruff, I., Sansing, L., Schulman, S., Selim, M., Sheth, K., Sprigg, N., Sunnerhagen, K., 2022. 2022 guideline for the management of patients with spontaneous intracerebral hemorrhage: A guideline from

- the american heart association/american stroke association. *Stroke* 53, E282–E361. doi:10.1161/STR.0000000000000407.
- Han, W., Kim, C., Ju, D., Shim, Y., Hwang, S.J., 2024. Advancing text-driven chest x-ray generation with policy-based reinforcement learning, in: *International Conference on Medical Image Computing and Computer-Assisted Intervention*, Springer. pp. 56–66.
- He, K., Zhang, X., Ren, S., Sun, J., 2016. Deep residual learning for image recognition, in: *Proceedings of the IEEE conference on computer vision and pattern recognition*, pp. 770–778.
- Ho, K.C., Scalzo, F., Sarma, K.V., Speier, W., El-Saden, S., Arnold, C., 2019. Predicting ischemic stroke tissue fate using a deep convolutional neural network on source magnetic resonance perfusion images. *Journal of Medical Imaging* 6, 026001–026001.
- Hori, M., Hagiwara, A., Goto, M., Wada, A., Aoki, S., 2021. Low-field magnetic resonance imaging: its history and renaissance. *Investigative radiology* 56, 669–679.
- Huang, H., Yang, G., Zhang, W., Xu, X., Yang, W., Jiang, W., Lai, X., 2021. A deep multi-task learning framework for brain tumor segmentation. *Frontiers in oncology* 11, 690244.
- Khatami, S.N., Gopalappa, C., 2021. A reinforcement learning model to inform optimal decision paths for hiv elimination. *Mathematical biosciences and engineering: MBE* 18, 7666.
- Kingma, D.P., Ba, J., 2014. Adam: A method for stochastic optimization. arXiv preprint arXiv:1412.6980 .
- Kool, D.R., Blickman, J.G., 2007. Advanced trauma life support®. abcde from a radiological point of view. *Emergency radiology* 14, 135–141.
- Kool, W., van Hoof, H., Welling, M., 2019. Buy 4 REINFORCE samples, get a baseline for free! URL: <https://openreview.net/forum?id=r11gTGL5DE>.
- Li, R., Pan, J., Zhu, Y., Ni, J., Rueckert, D., 2024. Classification, regression and segmentation directly from k-space in cardiac mri, in: *International Workshop on Machine Learning in Medical Imaging*, Springer. pp. 31–41.

- Liao, X., Li, W., Xu, Q., Wang, X., Jin, B., Zhang, X., Wang, Y., Zhang, Y., 2020. Iteratively-refined interactive 3d medical image segmentation with multi-agent reinforcement learning, in: Proceedings of the IEEE/CVF conference on computer vision and pattern recognition, pp. 9394–9402.
- Lin, D.J., Johnson, P.M., Knoll, F., Lui, Y.W., 2021. Artificial intelligence for mr image reconstruction: an overview for clinicians. *Journal of Magnetic Resonance Imaging* 53, 1015–1028.
- Liu, C., Xu, X., Hu, D., 2014. Multiobjective reinforcement learning: A comprehensive overview. *IEEE Transactions on Systems, Man, and Cybernetics: Systems* 45, 385–398.
- Liu, Y., Pang, Y., Jin, R., Hou, Y., Li, X., 2024. Reinforcement Learning and Transformer for Fast Magnetic Resonance Imaging Scan. *IEEE Transactions on Emerging Topics in Computational Intelligence* 8, 2310–2323. doi:10.1109/TETCI.2024.3358180.
- Maeland, E., 1988. On the comparison of interpolation methods. *IEEE Transactions on Medical Imaging* 7, 213–217. doi:10.1109/42.7784.
- Mao, A., Mohri, M., Zhong, Y., 2023. Cross-entropy loss functions: Theoretical analysis and applications, in: Proceedings of the 40th International Conference on Machine Learning, PMLR. pp. 23803–23828.
- Martinini, F., Mangia, M., Marchioni, A., Rovatti, R., Setti, G., 2022. A deep learning method for optimal undersampling patterns and image recovery for mri exploiting losses and projections. *IEEE Journal of Selected Topics in Signal Processing* 16, 713–724.
- Mazurek, M.H., Cahn, B.A., Yuen, M.M., Prabhat, A.M., Chavva, I.R., Shah, J.T., Crawford, A.L., Welch, E.B., Rothberg, J., Sacolick, L., et al., 2021. Portable, bedside, low-field magnetic resonance imaging for evaluation of intracerebral hemorrhage. *Nature communications* 12, 5119.
- Pineda, L., Basu, S., Romero, A., Calandra, R., Drozdal, M., 2020. Active mr k-space sampling with reinforcement learning, in: International Conference on Medical Image Computing and Computer-Assisted Intervention, Springer. pp. 23–33.

- Ravula, S., Levac, B., Jalal, A., Tamir, J.I., Dimakis, A.G., 2023. Optimizing sampling patterns for compressed sensing mri with diffusion generative models. arXiv preprint arXiv:2306.03284 .
- Ronneberger, O., Fischer, P., Brox, T., 2015. U-net: Convolutional networks for biomedical image segmentation, in: Medical image computing and computer-assisted intervention–MICCAI 2015: 18th international conference, Munich, Germany, October 5-9, 2015, proceedings, part III 18, Springer. pp. 234–241.
- Royal College of Radiologists, 2018. Standards for interpretation and reporting of imaging investigations. Technical Report. The Royal College of Radiologists. London, UK.
- Schlemper, J., Oktay, O., Bai, W., Castro, D.C., Duan, J., Qin, C., Hajnal, J.V., Rueckert, D., 2018. Cardiac mr segmentation from undersampled k-space using deep latent representation learning, in: Medical Image Computing and Computer Assisted Intervention–MICCAI 2018: 21st International Conference, Granada, Spain, September 16-20, 2018, Proceedings, Part I, Springer. pp. 259–267.
- Singhal, R., Sudarshan, M., Mahishi, A., Kaushik, S., Ginocchio, L., Tong, A., Chandarana, H., Sodickson, D.K., Ranganath, R., Chopra, S., 2023. On the feasibility of machine learning augmented magnetic resonance for point-of-care identification of disease. arXiv preprint arXiv:2301.11962 .
- Skalse, J., Hammond, L., Griffin, C., Abate, A., 2022. Lexicographic multi-objective reinforcement learning. arXiv preprint arXiv:2212.13769 .
- Sondik, E.J., 1971. The optimal control of partially observable Markov processes. Stanford University.
- Vlontzos, A., Alansary, A., Kamnitsas, K., Rueckert, D., Kainz, B., 2019. Multiple landmark detection using multi-agent reinforcement learning, in: Medical Image Computing and Computer Assisted Intervention–MICCAI 2019: 22nd International Conference, Shenzhen, China, October 13–17, 2019, Proceedings, Part IV 22, Springer. pp. 262–270.
- Wachinger, C., Rieckmann, A., Pölsterl, S., Initiative, A.D.N., et al., 2021. Detect and correct bias in multi-site neuroimaging datasets. Medical Image Analysis 67, 101879.

- Wang, G., Fessler, J.A., 2023. Efficient approximation of jacobian matrices involving a non-uniform fast fourier transform (nufft). *IEEE transactions on computational imaging* 9, 43–54.
- Wang, G., Luo, T., Nielsen, J.F., Noll, D.C., Fessler, J.A., 2022a. B-spline parameterized joint optimization of reconstruction and k-space trajectories (bjork) for accelerated 2d mri. *IEEE Transactions on Medical Imaging* 41, 2318–2330.
- Wang, J., Yang, Q., Yang, Q., Xu, L., Cai, C., Cai, S., 2022b. Joint optimization of cartesian sampling patterns and reconstruction for single-contrast and multi-contrast fast magnetic resonance imaging. *Computer Methods and Programs in Biomedicine* 226, 107150.
- Wang, Z., Bovik, A.C., Sheikh, H.R., Simoncelli, E.P., 2004. Image quality assessment: from error visibility to structural similarity. *IEEE transactions on image processing* 13, 600–612.
- Wu, Z., Yin, T., Sun, Y., Frost, R., van der Kouwe, A., Dalca, A.V., Bouman, K.L., 2024. Learning task-specific strategies for accelerated mri. *IEEE transactions on computational imaging* 10, 1040–1054.
- Xuan, K., Sun, S., Xue, Z., Wang, Q., Liao, S., 2020. Learning mri k-space subsampling pattern using progressive weight pruning, in: *Medical Image Computing and Computer Assisted Intervention–MICCAI 2020: 23rd International Conference, Lima, Peru, October 4–8, 2020, Proceedings, Part II* 23, Springer. pp. 178–187.
- Yen, C.Y., Singhal, R., Sharma, U., Ranganath, R., Chopra, S., Pinto, L., 2024. Adaptive sampling of k-space in magnetic resonance for rapid pathology prediction. *arXiv preprint arXiv:2406.04318* .
- Yiasemis, G., Sánchez, C.I., Sonke, J.J., Teuwen, J., 2024. On retrospective k-space subsampling schemes for deep mri reconstruction. *Magnetic Resonance Imaging* 107, 33–46.
- Yu, C., Liu, J., Nemati, S., Yin, G., 2021. Reinforcement learning in healthcare: A survey. *ACM Computing Surveys (CSUR)* 55, 1–36.
- Zbontar, J., Knoll, F., Sriram, A., Murrell, T., Huang, Z., Muckley, M.J., Defazio, A., Stern, R., Johnson, P., Bruno, M., et al., 2018. *fastmri*:

An open dataset and benchmarks for accelerated mri. arXiv preprint arXiv:1811.08839 .

Zeng, G., Guo, Y., Zhan, J., Wang, Z., Lai, Z., Du, X., Qu, X., Guo, D., 2021. A review on deep learning mri reconstruction without fully sampled k-space. *BMC Medical Imaging* 21, 195.

Zhang, D., Chen, B., Li, S., 2021. Sequential conditional reinforcement learning for simultaneous vertebral body detection and segmentation with modeling the spine anatomy. *Medical image analysis* 67, 101861.

Zhang, J., Zhang, H., Wang, A., Zhang, Q., Sabuncu, M., Spincemaille, P., Nguyen, T.D., Wang, Y., 2020. Extending loupe for k-space under-sampling pattern optimization in multi-coil mri, in: *Machine Learning for Medical Image Reconstruction: Third International Workshop, MLMIR 2020, Held in Conjunction with MICCAI 2020, Lima, Peru, October 8, 2020, Proceedings 3*, Springer. pp. 91–101.

Zhang, Z., Romero, A., Muckley, M.J., Vincent, P., Yang, L., Drozdal, M., 2019. Reducing uncertainty in undersampled mri reconstruction with active acquisition, in: *Proceedings of the IEEE/CVF conference on computer vision and pattern recognition*, pp. 2049–2058.

Zhao, R., Yaman, B., Zhang, Y., Stewart, R., Dixon, A., Knoll, F., Huang, Z., Lui, Y.W., Hansen, M.S., Lungren, M.P., 2022. fastmri+, clinical pathology annotations for knee and brain fully sampled magnetic resonance imaging data. *Scientific Data* 9, 152.

Zhao, Y., Wang, X., Che, T., Bao, G., Li, S., 2023. Multi-task deep learning for medical image computing and analysis: A review. *Computers in Biology and Medicine* 153, 106496.